Research Paper

Impact of Wall Impedance Phase Angle on Indoor Sound Field and Reverberation Parameters Derived from Room Impulse Response

Mirosław MEISSNER*, Tomasz G. ZIELIŃSKI

Institute of Fundamental Technological Research, Polish Academy of Sciences
Warsaw, Poland

*Corresponding Author e-mail: mmeissn@ippt.pan.pl

Accurate definition of boundary conditions is of crucial importance for room acoustic predictions because the wall impedance phase angle can affect the sound field in rooms and acoustic parameters applied to assess a room reverberation. In this paper, the issue was investigated theoretically using the convolution integral and a modal representation of the room impulse response for complex-valued boundary conditions. Theoretical considerations have been accompanied with numerical simulations carried out for a rectangular room. The case of zero phase angle, which is often assumed in room acoustic simulations, was taken as a reference, and differences in the sound pressure level and decay times were determined in relation to this case. Calculation results have shown that a slight deviation of the phase angle with respect to the phase equal to zero can cause a perceptual difference in the sound pressure level. This effect was found to be due to a change in modal frequencies as a result of an increase or decrease in the phase angle. Simulations have demonstrated that surface distributions of decay times are highly irregular, while a much greater range of the early decay time compared to the reverberation time range indicates that a decay curve is nonlinear. It was also found that a difference between the decay times predicted for the complex impedance and real impedance is especially clearly audible for the largest impedance phase angles because it corresponds approximately to 4 just noticeable differences for the reverberation metrics.

Keywords: room acoustics; complex wall impedance; indoor sound field; room impulse response; reverberation parameters.

1. Introduction

Acoustics of rooms has been studied for many years because a room behaviour in steady and transient states needs to be evaluated at the design phase and before acoustic treatments of rooms. Prediction of indoor sound field and determination of reverberation characteristics of rooms are not simple, and several theoretical and numerical methods of different complexity have been developed. These include statistical-acoustic methods (SUMMERS, 2012), the acoustic diffusion equation model (NAVARRO, ESCOLANO, 2015), geometrical acoustics methods such as the mirror source method (ARETZ *et al.*, 2014), and the ray-tracing techniques (WINKLER-SKALNA, NOWOŚWIAT, 2021), wave-based approaches such as the modal expansion method (DANCE, VAN BUUREN, 2013), the finite-element method (YOSHIDA *et al.*, 2020),

and the boundary element method (YASUDA *et al.*, 2020), the finite difference time domain method (MURPHY *et al.*, 2014), and meshless techniques (PRĘDKA, BRAŃSKI, 2020). The main acoustic elements employed to improve the acoustic quality of rooms are reflective surfaces, diffusers, and sound absorbing materials. The first two are mainly used to distribute indoor sound field energy, whereas the role of sound absorbers is reduction of sound levels and control of reverberation. The effect of sound absorbing walls on the indoor sound field can be fully characterised by the wall impedance. In the past, real-valued wall impedance approximations have been commonly used for room acoustic simulations (YOKOTA *et al.*, 2002; MEISSNER, 2008; PRISLAN *et al.*, 2016). However, since acoustic properties of sound absorbers are characterised by complex impedances (COX, D'ANTONIO, 2009), it is more correct to use complex-valued boundary

conditions in room acoustics modelling (Meissner, Wiśniewski, 2020; Szemela, Rdzanek, 2022). It is especially important for rooms of small volumes, where the wall impedance phase angle has a significant impact on the modal behaviour at low frequencies (Meissner, 2019).

Previous works examining the effect of the wall impedance phase angle on steady state and transient room responses have focused on improving the geometrical acoustics models. Suh and Nelson (1999) implemented the phase image model using the complex reflection coefficient to calculate the impulse response in two small and medium-sized rooms. They found significant differences between frequency response functions obtained for the complex wall impedance and in the case when it is replaced by the real-valued impedance that has the same normal absorption coefficient as the complex impedance. Jeong (2012) investigated real and complex-valued boundary conditions using the phased beam tracing method and found that the impedance phase angle affects the sound pressure level. In the study of Jeong *et al.* (2014), the phased beam tracing method was used to investigate the perceived reverberance for the wall impedance with different phase angles. It was found that, for uniform absorption settings, the non-zero impedance phase angle results in a perceptual difference in reverberance when compared to a zero-phase impedance. It was also shown that for typical rectangular room configurations with various types of absorptive ceilings, the impedance phase angle of the ceiling does not affect substantial changes in both the sound pressure level and early decay time.

In this study, theoretical and numerical models based on a modal approach are used to examine the effect of the wall impedance phase angle on indoor sound field and acoustic parameters employed to assess a room reverberation. In the theoretical model, the convolution integral and the room impulse response determined for complex-valued boundary conditions are applied. To find a decay curve that enables a prediction of decay times, a time-reverse integration of the squared room impulse response is used. The theoretical method is tested numerically for a room with internal damping provided by sound absorbing material evenly distributed over all room walls. In computer simulations, a wide range of impedance phase angle is tested, assuming that the non-zero phase impedance and the real impedance correspond to the same random incident absorption coefficient. Although the method applies to rooms of any shape, a rectangular enclosure was chosen as the test room because the modal behaviour of such a room has been thoroughly studied in the past. Among these studies, the works of Maa (1939), Hunt *et al.* (1939), and Nolan, Davy (2019) are of particular importance. Maa (1939) derived asymptotic formulas for the cumulative number of acoustic modes in a rectangular room. Hunt *et al.* (1939) examined the sound decay in rectangular rooms and the interaction of modes with different reverberation times. Nolan and Davy (2019) extended the existing modal theory for a reverberant sound field in rectangular rooms with almost hard walls to rectangular rooms whose walls may have different impedances and examined the orthogonality of spatial modal functions in this case.

2. Theoretical considerations

2.1. Boundary condition for complex wall impedance

An arbitrary shaped room with sound absorbing walls is considered. The sound field inside the room space is produced by a volume source. The room walls are assumed to be locally reacting, i.e. the normal velocity component u_n at any point on these walls depends only on the local pressure at that point. In this case the boundary condition is as follows:

$$\nabla p \cdot \mathbf{n} = -\rho \frac{\partial u_n}{\partial t} = -\frac{1}{c\zeta} \frac{\partial p}{\partial t} = -\frac{(\cos\mu - \mathrm{j}\sin\mu)}{c|\zeta|} \frac{\partial p}{\partial t}, \quad (1)$$

where p is the sound pressure, $\nabla = \mathbf{i}\partial/\partial x + \mathbf{j}\partial/\partial y + \mathbf{k}\partial/\partial z$ is the gradient vector operator, the dot is a scalar product, $\mathbf{n}$ is the outward normal vector, ρ is the air density, c is the sound speed, and $|\zeta|$ and μ are the magnitude and the phase angle of the normalised wall impedance ζ, respectively. It is assumed that absorbing properties of room walls are characterised by the random incidence absorption coefficient α which is related to the normalised wall impedance ζ by the following expression (Kuttruff, 2009):

$$\alpha = \frac{8}{|\zeta|^2}\cos\mu\left[|\zeta| + \frac{\cos(2\mu)}{\sin\mu}\arctan\left(\frac{|\zeta|\sin\mu}{1 + |\zeta|\cos\mu}\right)\right.$$

$$\left. - \cos\mu\ln\left(1 + 2|\zeta|\cos\mu + |\zeta|^2\right)\right]. \quad (2)$$

The complex wall impedance should fulfill the requirement of passivity, which means that the room walls do not supply energy to the sound field. Since $|\zeta|\cos\mu$ represents the wall resistance, this requirement is equivalent to the condition $-90° \le \mu \le 90°$. Calculation results obtained from Eq. (2), shown in Fig. 1, provide more details about the possible ranges of μ. The plots depict curves of constant values of α in a coordinate system, whose abscissa and ordinate are the phase angle and the magnitude of the impedance ζ, respectively. As can be seen, the phase angle μ possesses values from the range $\langle -\mu_{\max}, \mu_{\max}\rangle$ and $\mu_{\max}$ is strongly dependent on the absorption coefficient α. When room walls are assumed to be perfectly rigid, $\mu_{\max}$ reaches the maximum value of 90°. On the contrary, $\mu_{\max}$ is equal to zero degrees when the absorption coefficient
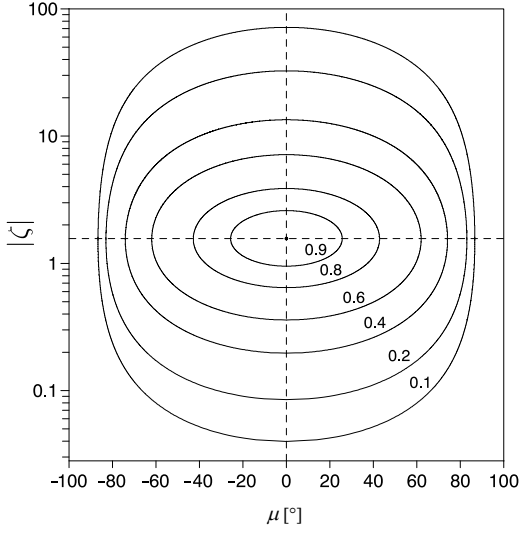
Fig. 1. Contours of constant values of the absorption coefficient α. The abscissa is the phase angle μ, and the ordinate is the magnitude $|\zeta|$ of the normalised wall impedance ζ.

is at its absolute maximum 0.951. In this case, a contour curve becomes the point which is located at the intersection of the lines $\mu = 0$ and $|\zeta| = 1.567$ indicated in Fig. 1 by dashed lines. A dependence of $\mu_{\max}$ on the absorption coefficient α is plotted in Fig. 2. As may be noted, large values of $\mu_{\max}$ substantially limit the range of possible values of the absorption coefficient. For example, when $\mu_{\max}$ is equal to $60°$, the values of α cannot be greater than 0.627.
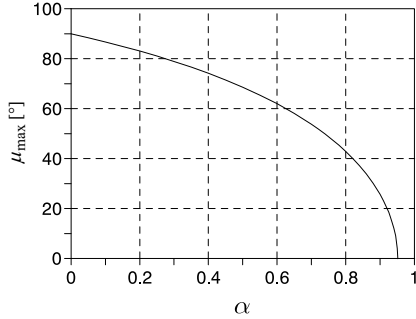

Fig. 2. Dependence of $\mu_{\max}$ on the absorption coefficient α.

2.2. Indoor sound field

The most convenient way of describing the indoor sound field is to use the room impulse response (RIR). The RIR is very useful in room acoustics because the knowledge of the RIR function $h(\mathbf{r}', \mathbf{r}, t)$, describing the pressure response at the receiving point $\mathbf{r} = (x, y, z)$ to the time impulse at the point $\mathbf{r}' = (x', y', z')$, enables to predict the room response to any sound source. If spatial and temporal properties of the source are described by the function $q(\mathbf{r}', t)$, the pressure response to this excitation can be determined using the convolution integral in the time domain (DAMELIN, MILLER, 2012):

$$p(\mathbf{r}, t) = \int\limits_V q(\mathbf{r}', t) * h(\mathbf{r}', \mathbf{r}, t)\, \mathrm{d}^3\mathbf{r}'$$

$$= \int\limits_{-\infty}^{t} \int\limits_V q(\mathbf{r}', \tau) h(\mathbf{r}', \mathbf{r}, t - \tau)\, \mathrm{d}^3\mathbf{r}'\, \mathrm{d}\tau, \quad (3)$$

where V is the room volume, the symbol $*$ denotes the convolution operation, and $\mathrm{d}^3\mathbf{r}'$ is the symbol for the volume element $\mathrm{d}^3\mathbf{r}' = \mathrm{d}x'\,\mathrm{d}y'\,\mathrm{d}z'$. Since the theoretical model is intended for the low-frequency range, the modal expansion method was used to determine the RIR function (MEISSNER, ZIELIŃSKI, 2020), and the result is as follows:

$$h(\mathbf{r}', \mathbf{r}, t) = c^2 \sum_{m=1}^{\infty} \frac{e^{-\xi_m t} \sin(\psi_m t) \Phi_m(\mathbf{r}') \Phi_m(\mathbf{r})}{\psi_m}, \quad (4)$$

where Φ_m are eigenfunctions, the modal coefficients ξ_m are expressed as:

$$\xi_m = r_m + \mathrm{j}\varphi_m = \frac{c}{2} \int\limits_S \frac{(\cos\mu - \mathrm{j}\sin\mu)\Phi_m^2}{|\zeta|}\, \mathrm{d}S, \quad (5)$$

where S is the surface of room walls, ψ_m are complex frequencies given by:

$$\psi_m = \Omega_m + \mathrm{j}\vartheta_m$$

$$= \sqrt{\frac{a_m + \sqrt{a_m^2 + b_m^2}}{2}} + \mathrm{j}\sqrt{\frac{-a_m + \sqrt{a_m^2 + b_m^2}}{2}}, \quad (6)$$

where $a_m = \omega_m^2 - r_m^2 + \varphi_m^2$, $b_m = -2r_m\varphi_m$, and ω_m are eigenfrequencies. The steady state pressure response to a point source located at $\mathbf{r}_0 = (x_0, y_0, z_0)$ can be found assuming that in Eq. (3) the source function has the form $q(\mathbf{r}', \tau) = Q\delta(\mathbf{r}' - \mathbf{r}_0)e^{\mathrm{j}\omega\tau}$, where ω is the source angular frequency and the amplitude Q is dependent on the source power W according to the formula $Q = \sqrt{8\pi\rho c W}$. Thus, after calculating the volume and time integral in Eq. (3), the formula for the steady state pressure amplitude P is found as:

$$P(\mathbf{r}) = Qc^2 \left\{ \left[\sum_{m=1}^{\infty} \frac{(\omega_m^2 - \omega^2 - 2\omega\varphi_m)\Phi_m(\mathbf{r}_0)\Phi_m(\mathbf{r})}{(\omega_m^2 - \omega^2 - 2\omega\varphi_m)^2 + 4r_m^2\omega^2} \right]^2 \right.$$

$$\left. + \left[\sum_{m=1}^{\infty} \frac{2\omega r_m \Phi_m(\mathbf{r}_0)\Phi_m(\mathbf{r})}{(\omega_m^2 - \omega^2 - 2\omega\varphi_m)^2 + 4r_m^2\omega^2} \right]^2 \right\}^{1/2}. \quad (7)$$

Equation (7) indicates that the pressure amplitude P depends on the source and receiver positions $\mathbf{r}_0$ and $\mathbf{r}$, the source frequency ω, the eigenfrequencies ω_m and, through the quantities r_m and φ_m, on the real and imaginary parts of the impedance ζ. Thus, for a specific location of a point source and a fixed source frequency, Eq. (7) makes it possible to determine the spatial distribution of the steady state pressure amplitude inside a room. On the other hand, Eq. (7) enables one to predict the transfer function (TF) between the source and receiver positions for different values of the impedance ζ.

2.3. Reverberation parameters

Decay times are the main parameters determining reverberant sound field, thus, they are commonly used to assess the acoustical quality of a room. For a theoretical description of a sound decay process in a room space, two methods are primarily applied. In the first method, the sound decay after switching off the pure tone sound excitation is analysed. In this case, a mathematical expression for a transient pressure response can be obtained from Eq. (3) assuming $q(\mathbf{r}', \tau) = Q\delta(\mathbf{r}' - \mathbf{r}_0)e^{j\omega\tau}$ and performing the time integration from $-\infty$ to zero. However, a presence of decaying modal vibrations in this response results in high temporal irregularity of pressure amplitude making it difficult to correctly predict the decay times. One solution to this problem is to use the discrete Hilbert transform to determine the envelope of decaying sound (MEISSNER, 2021). The second method for describing the sound decay process bases on the backward integration of the squared RIR. The time reverse integration results in a statistically stable estimate of a decay process since the obtained decay plot corresponds to an average over infinitely many decay curves that would be obtained from exciting the room with bandpass filtered noise (SCHROEDER, 1965). This method is commonly known as the Schroeder integration and it produces a smoothed decay plot from which the decay times are directly estimated.

The obtained RIR function can be used to predict the decay times after transforming the right hand side of Eq. (4) to the form:

$$h(\mathbf{r}', \mathbf{r}, t) = \sum_{m=1}^{\infty} \left[\alpha_m(t) + j\beta_m(t) \right] \Phi_m(\mathbf{r}') \Phi_m(\mathbf{r}), \quad (8)$$

where the functions $\alpha_m(t)$ and $\beta_m(t)$ are expressed by:

$$\alpha_m(t) = \frac{c^2 e^{-r_m t}}{\Omega_m^2 + \vartheta_m^2}$$

$$\cdot \left\{ \left[\Omega_m \sin(\varphi_m t) + \vartheta_m \cos(\varphi_m t) \right] \cos(\Omega_m t) \sinh(\vartheta_m t) \right.$$

$$\left. + \left[\Omega_m \cos(\varphi_m t) - \vartheta_m \sin(\varphi_m t) \right] \sin(\Omega_m t) \cosh(\vartheta_m t) \right\},$$

$$(9)$$

$$\beta_m(t) = \frac{c^2 e^{-r_m t}}{\Omega_m^2 + \vartheta_m^2}$$

$$\cdot \left\{ \left[\Omega_m \cos(\varphi_m t) - \vartheta_m \sin(\varphi_m t) \right] \cos(\Omega_m t) \sinh(\vartheta_m t) \right.$$

$$\left. - \left[\Omega_m \sin(\varphi_m t) + \vartheta_m \cos(\varphi_m t) \right] \sin(\Omega_m t) \cosh(\vartheta_m t) \right\}.$$

$$(10)$$

Since the RIR function is complex, the quantity which corresponds to the squared RIR is a modulus of $h(\mathbf{r}', \mathbf{r}, t)$ squared:

$$g(t) = |h(\mathbf{r}', \mathbf{r}, t)|^2 = \left[\sum_{m=1}^{\infty} \alpha_m(t) \Phi_m(\mathbf{r}') \Phi_m(\mathbf{r}) \right]^2$$

$$+ \left[\sum_{m=1}^{\infty} \beta_m(t) \Phi_m(\mathbf{r}') \Phi_m(\mathbf{r}) \right]^2. \quad (11)$$

The decay function L_d describing a sound energy decrease in the decibel scale is determined using a normalised version of the backward integration procedure:

$$L_d(t) = 10 \log \left[\frac{\int_t^{\infty} g(\tau) \, d\tau}{\int_0^{\infty} g(\tau) \, d\tau} \right]. \quad (12)$$

Based on temporal changes in the decay function, reverberation parameters such as the early decay time (EDT) and the reverberation time T_{30} can be evaluated. EDT is predicted from a decrease in L_d from 0 to -10 dB, multiplied by the factor of 6, whereas T_{30} is the decay time estimated from a drop in L_d from -5 to -35 dB, multiplied by the factor of 2.

3. Numerical study

The proposed method of predicting room acoustics on the basis of RIR calculations applies to rooms of any shape. However, to carry out numerical tests over a wider frequency band, a rectangular enclosure with small sound damping on walls was chosen for the test room because the modal behaviour of such an enclosure is well known and described. The assumed dimensions of the test room are as follows: $L_x = 7$ m, $L_y = 5$ m, $L_z = 3$ m (Fig. 3). Since they correspond to dimensions of lecture rooms or small music studios, a sound source representing, for example, the mouth of a speaker was located at the point: $x_0 = 1$ m, $y_0 = 2$ m, $z_0 = 1.6$ m. As shown by Eq. (4), space distribution of the RIR depends on values of the eigenfunctions Φ_m at the source and receiver positions. Since room walls were assumed to provide small sound
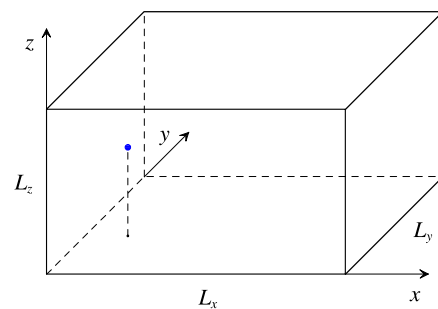
Fig. 3. Rectangular room under study together with the associated coordinate system. The source position is indicated by the blue point.

damping, the eigenfunctions Φ_m were approximated by eigenfunctions determined for rigid room walls:

$$\Phi_{n_x n_y n_z}(\mathbf{r}) = \sqrt{\frac{\epsilon_{n_x}\epsilon_{n_y}\epsilon_{n_z}}{V}} \cos\left(\frac{n_x \pi x}{L_x}\right)$$

$$\cdot \cos\left(\frac{n_y \pi y}{L_y}\right) \cos\left(\frac{n_z \pi z}{L_z}\right), \quad (13)$$

where the modal indices n_x, n_y, n_z are non-negative integers which are not simultaneously equal to zero, $\epsilon_{n_s} = 1$ if $n_s = 0$, and $\epsilon_{n_s} = 2$ if $n_s > 0$. The eigenfrequencies corresponding to these eigenfunctions can be calculated from the equation:

$$f_{n_x n_y n_z} = \frac{c}{2}\sqrt{\left(\frac{n_x}{L_x}\right)^2 + \left(\frac{n_y}{L_y}\right)^2 + \left(\frac{n_z}{L_z}\right)^2}. \quad (14)$$

The use of eigenfunctions for hard box modes in a series expansion of sound pressure means that the normal velocity component on the surface of a room's wall is equal to zero. As shown by Eq. (1), this condition is strictly met when the modulus of wall impedance tends to infinity or is satisfied approximately when this modulus is large enough. Therefore, the accuracy of the theoretical model should be good in the low frequency range, where sound absorbing materials are characterised by low absorption. This fact is confirmed by a high agreement between calculation results obtained from the theoretical model and FEM for large wall impedances (MEISSNER, ZIELIŃSKI, 2020).

In the test room, a sound damping was provided by an absorptive material with the impedance $\zeta = |\zeta|e^{j\mu}$, uniformly distributed on room walls. In order to ensure that these properties would be the same for the different phase angles μ, the value of $|\zeta|$ was chosen so that the random incident absorption coefficient α was kept constant. Therefore, in a developed numerical algorithm, the coefficient α and the phase angle μ were input parameters, and for the given values of α and μ, the impedance magnitude $|\zeta|$ was determined by the numerical solution of Eq. (2). In the numerical tests, it was assumed that the absorption coefficient takes the values of 0.05, 0.15, and 0.3, and for each of them, the magnitude $|\zeta|$ was computed for the angle μ varying in steps of $\pm 10°$. The values of $|\zeta|$ obtained in this way are listed in Table 1. For the absorption coefficient of 0.3 and the phase angle of $\pm 80°$, the impedance

Table 1. Magnitude $|\zeta|$ of the normalised wall impedance for selected values of the absorption coefficient α and the impedance phase angle μ.

α	μ								
	$0°$	$\pm10°$	$\pm20°$	$\pm30°$	$\pm40°$	$\pm50°$	$\pm60°$	$\pm70°$	$\pm80°$
0.05	150.4	148.1	141.3	130.1	115.0	96.4	74.7	50.8	25.1
0.15	45.5	44.8	42.7	39.3	34.6	28.9	22.2	14.8	6.7
0.3	19.8	19.5	18.5	17.0	14.9	12.3	9.3	5.8	–

magnitude $|\zeta|$ is not assigned because when μ is equal to $\pm 80°$, the value of α cannot be greater than 0.275 (Fig. 2).

3.1. Simulations of indoor sound field

To assess the perceived difference between spatial distributions of the pressure amplitude P for considered values of the angle μ, a quantity based on the pressure ratio was introduced:

$$D = \frac{20}{S_p} \int_{S_p} \left| \log\left[\frac{P(\mathbf{r})}{P_0(\mathbf{r})}\right] \right| \, \mathrm{d}S, \quad (15)$$

where S_p is the size of the horizontal observation plane and P_0 is the pressure amplitude for μ equal to zero. The use of an absolute value in the integrand guarantees that the ratios $P/P_0 = a$ and $P/P_0 = a^{-1}$, where a is any positive number, have identical contribution to the integral. The parameter D is quantified in decibels and when D is equal to 0 dB, the distributions of P and P_0 on the observation plane are exactly the same.

The pressure amplitude P was computed on the observation plane located at the distance $z = 1.2$ m above the floor of the test room. Such a distance approximately corresponds to the position of ears of seated listeners. Simulations were run on the computational grid with $N = 3621$ grid points regularly spaced on the observation plane. Therefore, the calculation of the parameter D was carried out according to the formula:

$$D = \frac{20}{N} \sum_{n=1}^{N} \left| \log\left[\frac{P(\mathbf{r}_n)}{P_0(\mathbf{r}_n)}\right] \right|, \quad (16)$$

where $\mathbf{r}_n$ is the grid point coordinate. Calculations of D were performed for the source frequency f of 100 Hz, 250 Hz, and 500 Hz and the results obtained are presented in Fig. 4 in the form of bar charts. These data indicate that the spatial distribution of the pressure amplitude P is very sensitive to changes in the phase angle μ because already for μ of $\pm 20°$ the parameter D is greater than 1 dB which exceeds the just noticeable difference (JND) in the sound pressure level for a tone frequency from 70 Hz to 1000 Hz and the pressure level greater than or equal to 40 dB (LONG, 2014). For the phase angle greater than $20°$ or smaller than $-20°$, an increase in parameter D is observed, and its greatest values of 5–7 dB occur for the highest values of μ. An explanation of why the parameter D reaches such great values can be found in Figs 5 and 6 depicting distributions of P on the observation plane for the source frequency of 100 Hz and 250 Hz, the absorption coefficient of 0.05, and the phase angle equal to $0°$, $\pm 50°$, $\pm 80°$. These figures show that changes in the phase angle result in modification of both the amplitude P and its distribution on the observation plane. The exception is the case: $f = 100$ Hz and $\mu = 50°$, where the value of D of about 3 dB is due only to a decrease in P
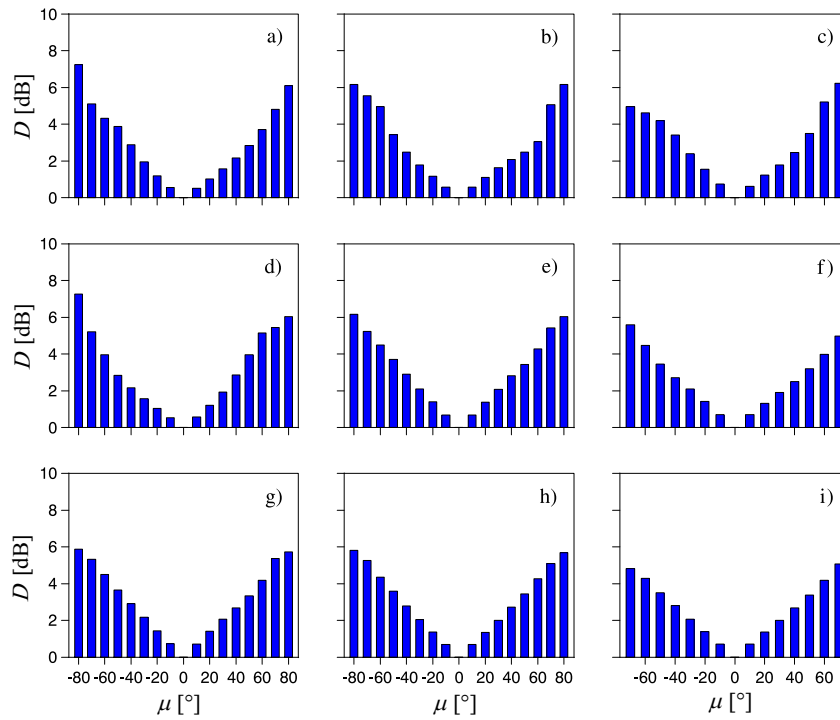
Fig. 4. Dependence of the parameter D on the impedance phase angle μ for the source frequency f of 100 Hz (a), (b), (c), 250 Hz (d), (e), (f), and 500 Hz (g), (h), (i). The absorption coefficient α equals 0.05 (a), (d), (g), 0.15 (b), (e), (h), and 0.3 (c), (f), (i).
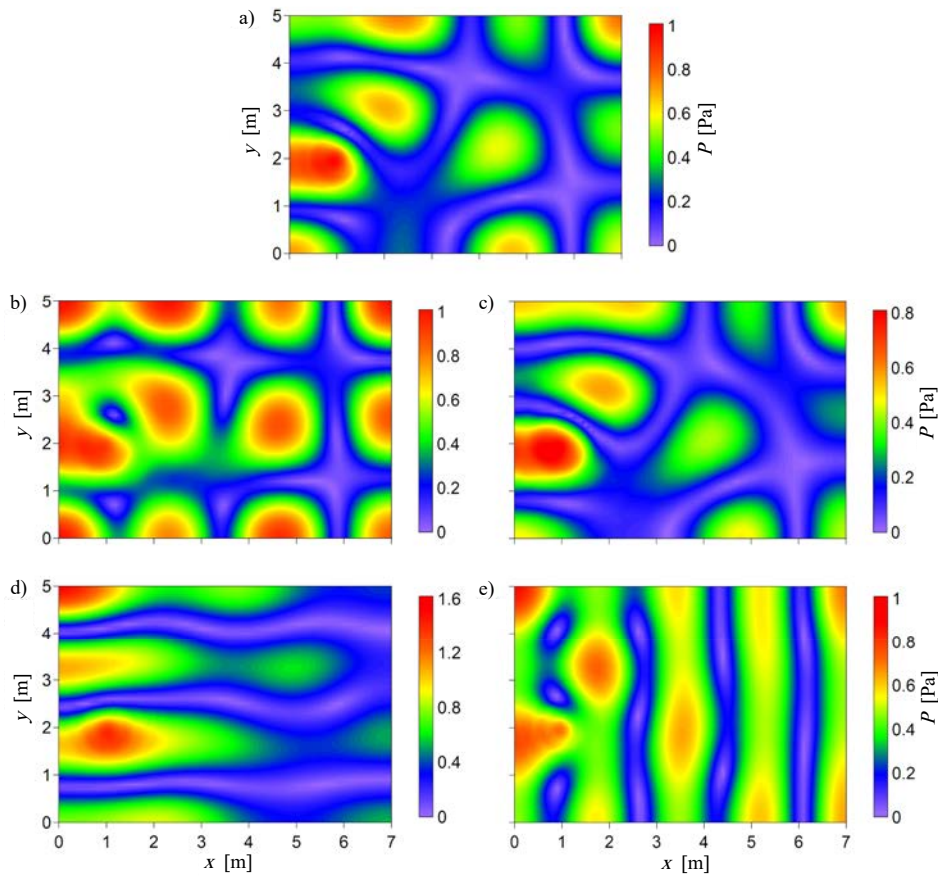

Fig. 5. Distributions of the pressure amplitude P on the observation plane for the source frequency f of 100 Hz, the absorption coefficient α of 0.05, and the impedance phase angle μ equal to: a) 0°, b) −50°, c) 50°, d) −80°, e) 80°.
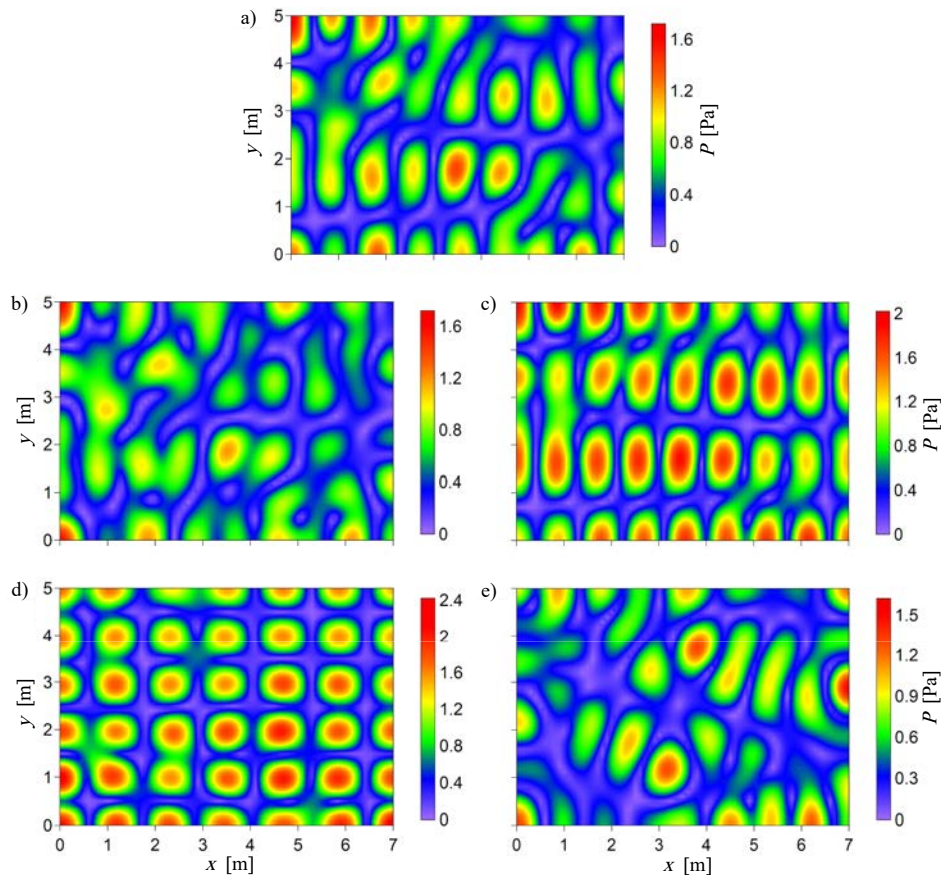
Fig. 6. Distributions of the pressure amplitude P on the observation plane for the source frequency f of 250 Hz, the absorption coefficient α of 0.05, and the impedance phase angle μ equal to: a) $0°$, b) $-50°$, c) $50°$, d) $-80°$, e) $80°$.

(Fig. 5c). The most regular distribution of the pressure amplitude was obtained for $f = 250$ Hz and $\mu = -80°$ (Fig. 6d). An analysis of calculation data revealed that this distribution corresponds to the distribution of P computed for the room mode $(6, 5, 2)$, i.e. the mode with indices: $n_x = 6$, $n_y = 5$, $n_z = 2$. The frequency of this mode, calculated from Eq. (14), is 253.17 Hz, so it clearly differs from the source frequency.

To elucidate this problem, the transfer functions for the phase angle μ of $0°$ and $-80°$ were computed at the receiving point: $x = 4.7$ m, $y = 2$ m, and $z = 1.2$ m, where for $\mu = -80°$ there is a local maximum of the pressure amplitude P (Fig. 6d). A comparison of TFs calculated in the frequency band 220–280 Hz is shown in Fig. 7. The dominant peak in the TF for $\mu = 0°$ corresponds to the mode $(6, 5, 2)$. However, when μ drops to $-80°$, the frequency of this peak changes to 250.3 Hz, making this mode dominant in the distribution of the pressure amplitude. Such a behaviour can be explained using Eq. (7). This equation shows that peaks of the pressure amplitude P occur near source frequencies:

$$\omega = \sqrt{\omega_m^2 + \varphi_m^2} - \varphi_m. \tag{17}$$

On the other hand, the relationship between φ_m and the phase angle μ is given by Eq. (5), and this equation
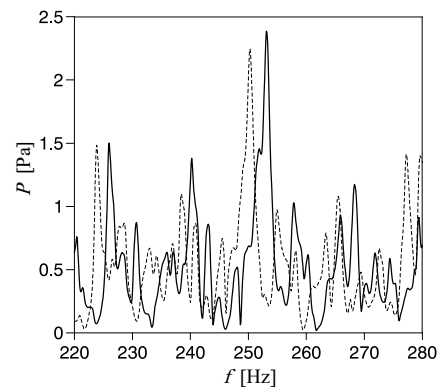

Fig. 7. Comparison of TFs computed at the receiving point: $x = 4.7$ m, $y = 2$ m, $z = 1.2$ m, for the absorption coefficient α of 0.05, and the impedance phase angle μ equal to: $0°$ (thick solid line) and $-80°$ (thin dashed line).

indicates that when μ is negative, the pressure peak frequency is lower than the peak frequency for μ equal to zero.

3.2. Predictions of decay times

In the numerical study, the early decay time (EDT) and the reverberation time T_{30} were predicted on the

basis of the temporal changes in the decay function L_d which is defined by Eq. (12). A method for determining the EDT and T_{30} was based on finding fit lines to appropriate parts of the function L_d and it was realised by the linear regression. To display the dependence of the decay times on the sound frequency, the function $g(t)$ corresponding to the squared RIR was bandpass filtered to yield the decay function L_d for the octave bands with the centre frequency from 63 Hz to 1000 Hz. Since $g(t)$ is determined by a series, the filtering algorithm was realised by summing such components of the series for which the eigenfrequency ω_m satisfies the condition $\omega_l < \omega_m < \omega_u$, where ω_l and ω_u are the lower and upper limits of the octave bands.

Figure 8 shows exemplary results of calculating the decay function L_d together with the predicted values of the decay times EDT and T_{30}. The graphs illustrate temporal changes in L_d at the receiving point: $x = 3$ m, $y = 4$ m, $z = 1.2$ m, located on the observation plane for the octave bands with the centre frequency from 63 Hz to 500 Hz, and the phase angle μ of $0°$ (solid lines) and $80°$ (dashed lines). The values of the EDT and T_{30} at the top correspond to the phase angle of $0°$. The data in Fig. 8 prove that a change of μ from $0°$ to $80°$ results in a decrease in the reverberation time T_{30}. Moreover, the values of T_{30} decrease with increasing the octave band centre frequency. This regularity results from the fact that in the RIR determined for a rectangular room, the share of modes with a lower modal reverberation time increases with the modal frequency (MEISSNER, 2017). As shown in Fig. 8, in almost all cases the values of EDT and T_{30} are close to each other, suggesting a nearly exponential nature of the sound decay. However, for the octave band 125 Hz and the phase angle of $0°$, changes in the decay function L_d are highly
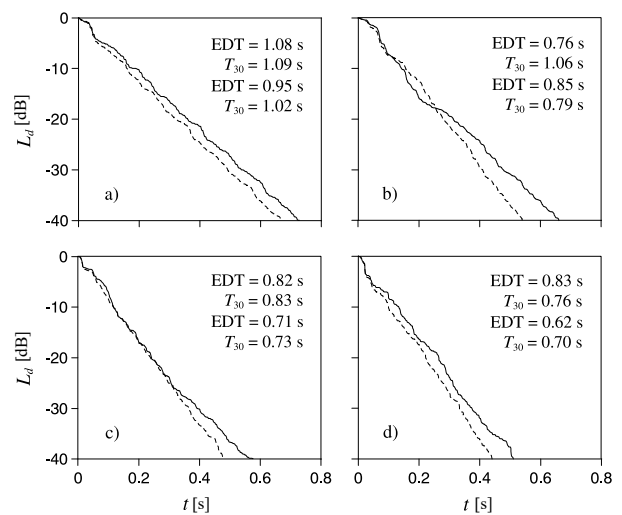
Fig. 8. Time dependence of the decay function L_d at the receiving point: $x = 3$ m, $y = 4$ m, $z = 1.2$ m, for the absorption coefficient α of 0.15, and the impedance phase angle μ of $0°$ (solid lines), $80°$ (dashed lines), for the octave bands: a) 63 Hz, b) 125 Hz, c) 250 Hz, d) 500 Hz. Values of the EDT and T_{30} at the top correspond to the phase angle of $0°$.

nonlinear, resulting in a significant difference between EDT and T_{30} (Fig. 8b). This kind of sound decay is concave in nature because it is characterised by a fast early decay rate and a slow late decay rate.

Equation (11) indicates that the decay function L_d depends on the receiver and source coordinates $\mathbf{r}$ and $\mathbf{r}_0$. Since the source position is fixed ($x_0 = 1$ m, $y_0 = 2$ m, $z_0 = 1.6$ m), the developed method allows to predict changes in EDT and T_{30} on the observation plane ($z = 1.2$ m). Exemplary calculation data are shown in Fig. 9. These results were obtained for the oc-
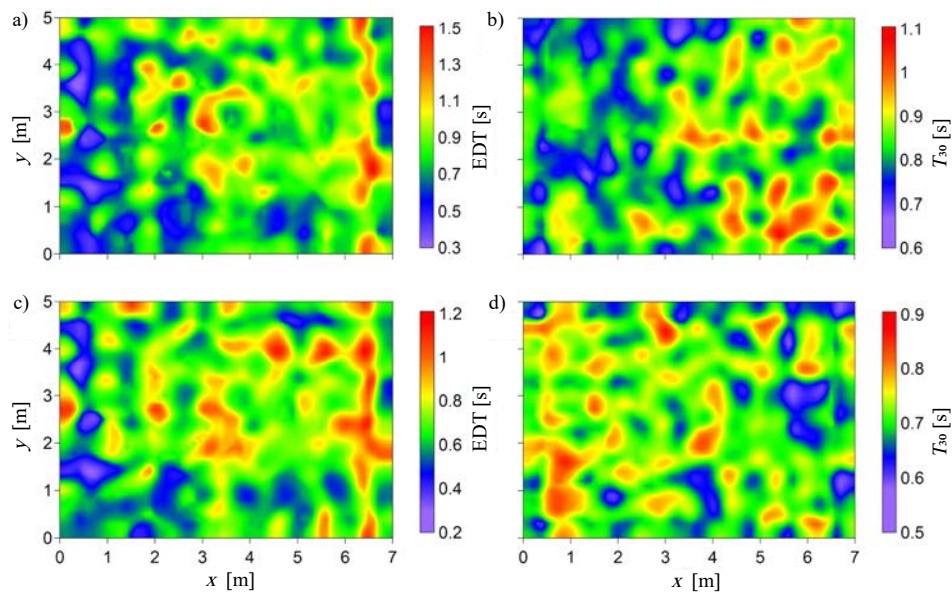
Fig. 9. Distributions of the decay times EDT and T_{30} on the observation plane for the absorption coefficient α of 0.15, and the impedance phase angle μ of: a), b) $0°$ and c), d) $80°$. Octave band 250 Hz.

tave band 250 Hz, the absorption coefficient α of 0.15, and the phase angle μ of 0° and 80°. As can be seen, surface distributions of EDT and T_{30} are highly irregular and there is significant difference between the distributions of T_{30} obtained for the phase angle equal to 0° and 80°. Another interesting observation resulting from Fig. 9 is a much larger range of the early decay time compared to the reverberation time range. This finding proves that the decay curve is nonlinear and its shape may be concave (EDT much smaller than T_{30}) or convex (EDT much greater than T_{30}).

Since the decay times EDT and T_{30} vary from point to point on the observation plane, an indicator which is adequate to quantify the impact of the impedance phase angle μ on the decay times is the mean relative difference E defined as:

$$E = \frac{1}{N} \sum_{n=1}^{N} \frac{|T(\mathbf{r}_n) - T_0(\mathbf{r}_n)|}{T_0(\mathbf{r}_n)} \cdot 100\%, \qquad (18)$$

where the quantities T and T_0 represent the EDT or T_{30}, and T_0 is determined for μ equal to zero, and the coordinate $\mathbf{r}_n$, as before, determines a grid point position on the observation plane. It is worth adding here that audible differences in the decay times are typically identified using the just noticeable difference (JND) for the reverberation metrics. This parameter is defined as the minimum change in the decay time that can be readily perceived and for the EDT and T_{30} the generally accepted value of the JND is 5% (HAK et al., 2012).

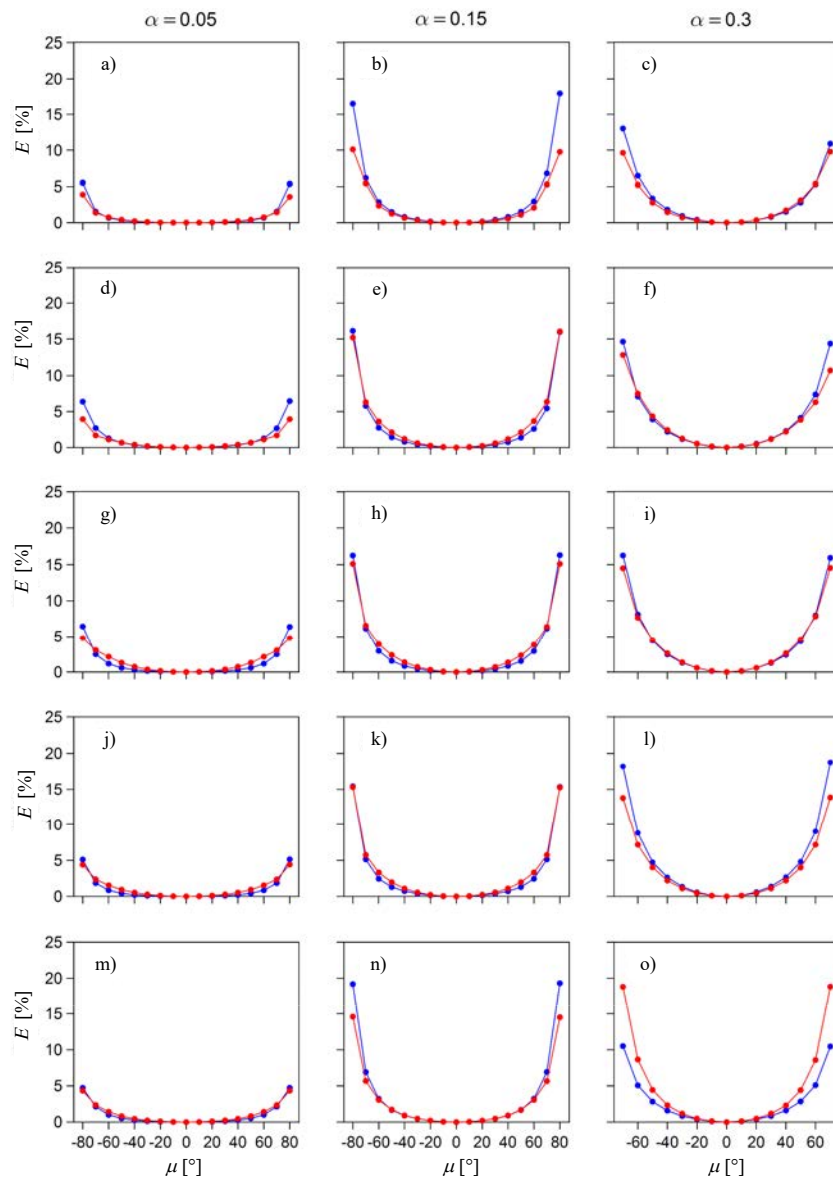Figure 10 depicts changes in the parameter E with the impedance phase angle μ in the considered octave

Fig. 10. Dependence of the parameter E on the impedance phase angle μ for the early decay time EDT (blue lines) and the reverberation time T_{30} (red lines), for the octave bands: 63 Hz (a)–(c), 125 Hz (d)–(f), 250 Hz (g)–(i), 500 Hz (j)–(l), 1000 Hz (m)–(o), and the absorption coefficient α equal to 0.05, 0.15, and 0.3.

bands for the assumed values of the absorption coefficient α. Based on these data, it can be concluded that for α of 0.05 the change in μ from zero to $\pm 80°$ may be noticeable only for the EDT because in this case the parameter E is around 6%, which is slightly above the JND. As could be expected, a much greater influence of μ on the decay times is noted for the absorption coefficient α of 0.15 and 0.3. Indeed, as can be seen from Fig. 10, the EDT and T_{30} are not significantly influenced by the phase angle μ, when its values are from $-60°$ to $60°$ for α of 0.15 and from $-50°$ to $50°$ for α of 0.3. For the remaining values of μ, the parameter E is greater than 5% and in extreme cases it reaches values around 19% (Figs 10n and 10o). Such a difference between the decay times should be especially clearly audible because it corresponds to approximately 4 JNDs.

4. Conclusions

Proper selection of the boundary conditions is critical in room acoustics modelling because the phase of wall impedance can have a significant impact on modal behaviour of a room. However, this phase is difficult to estimate from energy parameters such as the normal or random incident absorption coefficients, therefore real-valued boundary conditions are predominantly used in room acoustic simulations. In this study, a room acoustics model based on a modal approach was used to investigate to what extent the replacement of the complex wall impedance with the real impedance affects the indoor sound field and acoustic measures employed for quantifying a room reverberation.

In order to determine the indoor sound field, the convolution integral and the room impulse response for complex-valued boundary conditions were applied. Distributions of sound pressure levels in terms of the phase angle were simulated for a fixed value of the random incident absorption coefficient. This requirement ensures that absorption properties of the room will be the same for different values of the phase angle. The calculation results have shown that the phase angle greater than $20°$ or smaller than $-20°$ results in a perceptual difference in the sound pressure level when compared to a zero-phase impedance. This effect was found to be caused by a change in the modal frequencies and can be explained as follows. When the phase angle is negative, the sound waves are reflected from a virtual wall situated at some distance behind the real wall. This means that the acoustical volume of a room is greater than the physical volume, thus causing the modal frequencies to shift towards the lower frequencies.

A decay curve allowing to predict the early decay time (EDT) and the reverberation time T_{30} was found using a time-reverse integration of the squared room impulse response. As shown by the simulation data, the surface distributions of the decay times are highly irregular. Moreover, a significant difference is observed between the distributions of T_{30} obtained for the phase angle equal to $0°$ and $80°$. A much greater range of early decay time compared to the reverberation time range indicates that the decay curve is nonlinear and its shape may be concave (EDT much smaller than T_{30}) or convex (EDT much greater than T_{30}). Based on the simulation data, it can also be concluded that the differences between the decay times predicted for the complex impedance and real impedance should be especially clearly audible when the absolute value of the phase angle is $80°$ for the absorption coefficient of 0.15 and is equal to or greater than $60°$ for the absorption coefficient of 0.3.

Acknowledgments

References

1. Aretz M., Dietrich P., Vorländer M. (2014), Application of the mirror source method for low frequency sound prediction in rectangular rooms, *Acta Acustica united with Acustica*, **100**(2): 306–319, doi: 10.3813/AAA.918710.

2. Collins P.J. (2006), *Differential and Integral Equations*, Oxford University Press, New York.

3. Cox T., D'Antonio P. (2009), *Acoustic Absorbers and Diffusers: Theory, Design, and Application*, 2nd ed., Taylor & Francis, New York, doi: 10.4324/9781482266412.

4. Damelin S.B., Miller W. Jr (2012), *The Mathematics of Signal Processing*, Cambridge University Press, New York.

5. Dance S., Van Buuren G. (2013), Effects of damping on the low-frequency acoustics of listening rooms based on an analytical model, *Journal of Sound and Vibration*, **332**(25): 6891–6904, doi: 10.1016/j.jsv.2013.07.011.

6. Hak C.C.J.M., Wenmaekers R.H.H.C., van Luxemburg L.C.J. (2012), Measuring room impulse responses: impact of the decay range on derived room acoustic parameters, *Acta Acustica united with Acustica*, **98**(6): 907–915, doi: 10.3813/AAA.918574.

7. Hunt F.V., Beranek L.L., Maa D.Y. (1939), Analysis of sound decay in rectangular rooms, *The Journal of the Acoustical Society of America*, **11**(1): 80–94, doi: 10.1121/1.1916010.

8. JEONG C.-H. (2012), Absorption and impedance boundary conditions for phased geometrical acoustics methods, *The Journal of the Acoustical Society of America*, **132**(4): 2347–2358, doi: 10.1121/1.4740494.

9. JEONG C.-H., LEE D., SANTURETTE S., IH J.-G. (2014), Influence of impedance phase angle on sound pressures and reverberation times in a rectangular room, *The Journal of the Acoustical Society of America*, **135**(2): 712–723, doi: 10.1121/1.4861839.

10. KUTTRUFF H. (2009), *Room Acoustics*, 5th ed., Spon Press, New York.

11. LONG M. (2014), *Architectural Acoustics*, 2nd ed., Elsevier Academic Press, New York.

12. MAA D.-Y. (1939), Distribution of eigentones in a rectangular chamber at low frequency range, *The Journal of the Acoustical Society of America*, **10**(3): 235–238, doi: 10.1121/1.1915981.

13. MEISSNER M. (2008), Influence of wall absorption on low-frequency dependence of reverberation time in room of irregular shape, *Applied Acoustics*, **69**(7): 583–590, doi: 10.1016/j.apacoust.2007.02.004.

14. MEISSNER M. (2017), Acoustics of small rectangular rooms: Analytical and numerical determination of reverberation parameters, *Applied Acoustics*, **120**: 111–119, doi: 10.1016/j.apacoust.2017.01.020.

15. MEISSNER M. (2019), Prediction of low-frequency sound field in rooms with complex-valued boundary conditions on walls, *Vibrations in Physical Systems*, **30**(1): 2019127.

16. MEISSNER M. (2021), Application of modal expansion method for sound prediction in enclosed spaces subjected to boundary excitation, *Journal of Sound and Vibration*, **500**: 116041, doi: 10.1016/j.jsv.2021.116041.

17. MEISSNER M., WIŚNIEWSKI K. (2020), Investigation of damping effects on low-frequency steady-state acoustical behaviour of coupled spaces, *Royal Society Open Science*, **7**(8): 200514, doi: 10.1098/rsos.200514.

18. MEISSNER M., ZIELIŃSKI T.G. (2020), Low-frequency prediction of steady-state room response for different configurations of designed absorbing materials on room walls, [in:] *Proceedings of the 29th International Conference on Noise and Vibration Engineering (ISMA 2020) and the 8th International Conference on Uncertainty in Structural Dynamics (USD 2020)*, pp. 463–477.

19. MURPHY D.T, SOUTHERN A., SAVIOJA L. (2014), Source excitation strategies for obtaining impulse responses in finite difference time domain room acoustics simulation, *Applied Acoustics*, **82**: 6–14, doi: 10.1016/j.apacoust.2014.02.010.

20. NAVARRO J.M., ESCOLANO J. (2015), Simulation of building indoor acoustics using an acoustic diffusion equation model, *Journal of Building Performance Simulation*, **8**(1): 3–14, doi: 10.1080/19401493.2013.850534.

21. NOLAN M., DAVY J.L. (2019), Two definitions of the inner product of modes and their use in calculating non-diffuse reverberant sound fields, *The Journal of the Acoustical Society of America*, **145**(6): 3330–3340, doi: 10.1121/1.5109662.

22. PRĘDKA E., BRAŃSKI A. (2020), Analysis of the room acoustics with impedance boundary conditions in the full range of acoustic frequencies, *Archives of Acoustics*, **45**(1): 85–92, doi: 10.24425/aoa.2020.132484.

23. PRISLAN R., VEBLE G., SVENŠEK D. (2016), Raytrace modeling of acoustic Green's function based on the semiclassical (eikonal) approximation, *The Journal of the Acoustical Society of America*, **140**(4): 2695–2702, doi: 10.1121/1.4964295.

24. SCHROEDER M.R. (1965), New method of measuring reverberation time, *The Journal of the Acoustical Society of America*, **37**(3): 409–412, doi: 10.1121/1.1909343.

25. SUH J.S., NELSON P.A. (1999), Measurement of transient response of rooms and comparison with geometrical acoustic models, *The Journal of the Acoustical Society of America*, **105**(4): 2304–2317, doi: 10.1121/1.426837.

26. SUMMERS J.E. (2012), Accounting for delay of energy transfer between coupled rooms in statistical-acoustics models of reverberant-energy decay, *The Journal of the Acoustical Society of America*, **132**(2): 129–134, doi: 10.1121/1.4734591.

27. SZEMELA K., RDZANEK W. (2022), The influence of an impedance obstacle on the acoustic field inside a rectangular room, *Journal of Vibration and Acoustics*, **144**(2): 021005, doi: 10.1115/1.4051587.

28. WINKLER-SKALNA A., NOWOŚWIAT A. (2021), Use of n-perturbation interval ray tracing method in predicting acoustic field distribution, *Applied Mathematical Modelling*, **93**: 426–442, doi: 10.1016/j.apm.2020.12.028.

29. YASUDA Y., SAITO K., SEKINE H. (2020), Effects of the convergence tolerance of iterative methods used in the boundary element method on the calculation results of sound fields in rooms, *Applied Acoustics*, **157**: 106997, doi: 10.1016/j.apacoust.2019.08.003.

30. YOKOTA T., SAKAMOTO S., TACHIBANA H. (2002), Visualization of sound propagation and scattering in rooms, *Acoustical Science and Technology*, **23**(1): 40–46, doi: 10.1250/ast.23.40.

31. YOSHIDA T., OKUZONO T., SAKAGAMI K. (2020), Time domain room acoustic solver with fourth-order explicit FEM using modified time integration, *Applied Sciences*, **10**(11): 3750, doi: 10.3390/app10113750.